Received 18 June 2023; accepted 26 June 2023. Date of publication 11 July 2023; date of current version 31 July 2023.

Digital Object Identifier 10.1109/OJCOMS.2023.3292357

Reconfigurable Intelligent Surfaces: Interplay of Unit Cell and Surface-Level Design and Performance Under Quantifiable Benchmarks

AMMAR RAFIQUE [1], NAVEED UL HASSAN [2] (Senior Member, IEEE), MUHAMMAD ZUBAIR [1] (Senior Member, IEEE), IJAZ HAIDER NAQVI [2] (Senior Member, IEEE), MUHAMMAD QASIM MEHMOOD [1] (Senior Member, IEEE), MARCO DI RENZO [3] (Fellow, IEEE), MÉROUANE DEBBAH [4,5] (Fellow, IEEE), AND CHAU YUEN [6] (Fellow, IEEE)

[1]Electrical Engineering Department, Information Technology University, Lahore 54600, Pakistan

[2]Department of Electrical Engineering, Lahore University of Management Sciences, Lahore 54792, Pakistan

[3]Université Paris-Saclay, CNRS, CentraleSupélec, Laboratoire des Signaux et Systemes, 91192 Gif-sur-Yvette, France

[4]Center for 6G Technology, Khalifa University of Science and Technology, Abu Dhabi, UAE

[5]CentraleSupélec, University ParisSaclay, 91192 Gif-sur-Yvette, France

[6]School of Electrical and Electronics Engineering, Nanyang Technological University, Singapore

CORRESPONDING AUTHORS: N. UL HASSAN, M. ZUBAIR, AND M. DI RENZO (e-mail: naveed.hassan@lums.edu.pk; muhammad.zubair@itu.edu.pk; marco.di-renzo@universite-paris-saclay.fr)

This work was supported in part by the Ministry of Education, Singapore, under its MOE Tier 2 under Award MOE-T2EP50220-0019; in part by the Science and Engineering Research Council of A*STAR (Agency for Science, Technology and Research) Singapore, under Grant M22L1b0110; and in part by the LUMS Faculty Initiative Fund (FIF). The work of Marco Di Renzo was supported in part by the European Commission through the H2020 ARIADNE Project under Grant 871464, through the H2020 RISE-6G Project under Grant 101017011, and in part by the Agence Nationale de la Recherche (ANR PEPR-5G and Future Networks) under Grant NF-PERSEUS and Grant 22-PEFT-004.

ABSTRACT The ability of reconfigurable intelligent surfaces (RIS) to produce complex radiation patterns in the far-field is determined by various factors, such as the unit cell's design, spatial arrangement, tuning mechanism, the communication and control circuitry's complexity, and the illuminating source's type (point/planewave). Research on RIS has been mainly focused on two areas: first, the optimization and design of unit cells to achieve desired electromagnetic responses within a specific frequency band, and second, exploring the applications of RIS in various settings, including system-level performance analysis. The former does not assume any specific full radiation pattern on the surface level, while the latter does not consider any particular unit cell design. Both approaches largely ignore the complexity and power requirements of the RIS control circuitry. As we progress toward the fabrication and use of RIS in real-world settings, it is becoming increasingly necessary to consider the interplay between the unit cell design, the required surface-level radiation patterns, the control circuit's complexity, and the power requirements concurrently. In this paper, we propose a benchmarking framework comprising a set of simple and complex radiation patterns. Using full-wave simulations, we compare the relative performance of various RISs made from unit cell designs that use PIN diodes as control elements in producing the full radiation patterns in the far-field of the RIS under point/planewave source assumptions. We also analyze the control circuit complexity and power requirements and explore the tradeoffs of various designs.

INDEX TERMS 6G, RIS, unit cell.

I. INTRODUCTION

IN 6G wireless communication systems, Reconfigurable Intelligent Surfaces (RIS) and Holographic Multiple Input Multiple Output (HMIMO) systems are expected to provide an intelligent and software reconfigurable paradigm for adapting to the changes of the wireless environment [1], [2], [3], [4], [5], [6]. In particular, RIS will enable controlling the electromagnetic (EM) waves as they pass through

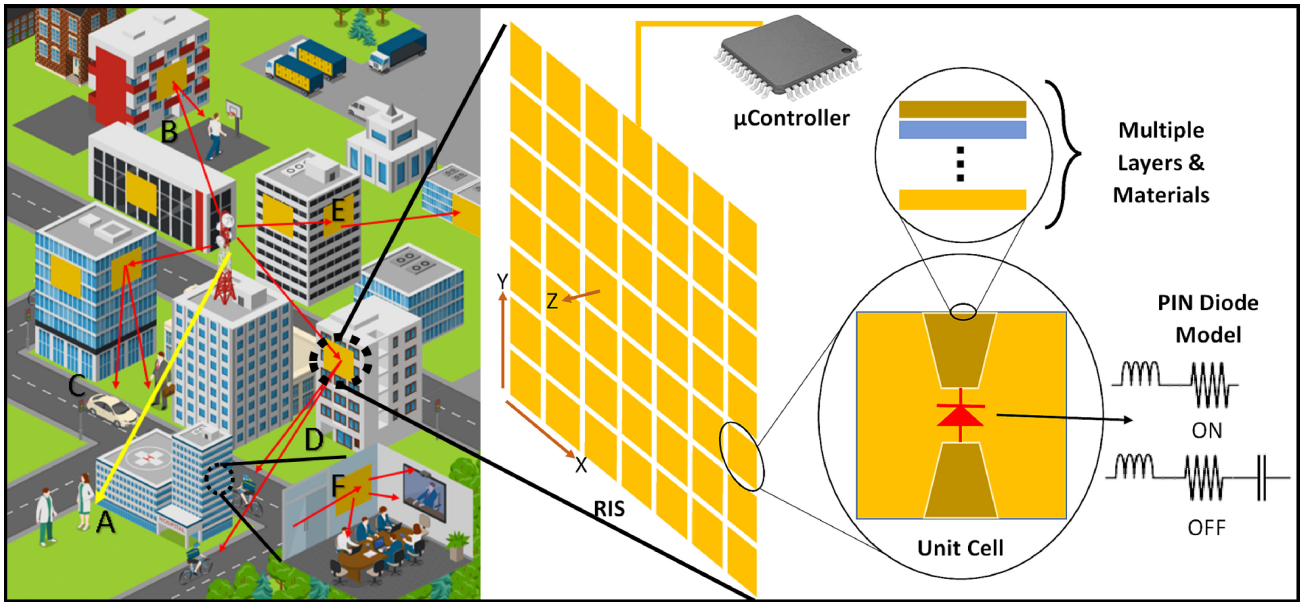

FIGURE 1. Example of an RIS-assisted urban environment.

the channel. It is expected that multiple geographically spread RISs will make the radio environment smart [7], while stacked intelligent surfaces and those composed of multifunctional layers will be able to perform wave-based calculation and signal processing [8], [9].

A popular design of an RIS includes a basic planar microstructure called a unit cell equipped with integrated electronic components such as diodes to allow the tuning of the magnitude and phase of the incident EM waves [10]. A thin surface is fabricated by repeating the unit cells at sub-wavelength periodic intervals. In this paper, we consider such an RIS comprising a sufficiently large number of unit cells. The RIS is expected to generate complex radiation patterns in a smart urban environment.

Various indoor and outdoor application scenarios of RIS-assisted wireless communications are illustrated in Figure 1. The typical structure of a unit cell, a PIN diode with ON/OFF control, the lumped-element models of the PIN diode, an RIS comprising of multiple unit cells, and a micro-controller to turn ON/OFF the PIN diodes for the generation of specified radiation patterns are also shown in this figure. Non-Line of Sight (NLoS) scenarios dominate urban environments where buildings often block the signals. In such situations, single beam steering and multi-beam forming with equal/unequal power levels at different angles may be achieved with the help of an RIS to reduce outages and improve the spectral efficiency [11], [12].

The near-field of an antenna or a unit cell is conventionally defined up to $\frac{2D^2}{\lambda}$ meters from the antenna or the unit cell, where D is the minimal diameter of a sphere that encloses the antenna or the unit cell, and λ is the wavelength [13]. Assuming that the RIS has N^2 unit cells, the near-field region of an RIS is N^2 times larger than the near-field boundary of a unit cell. Therefore, the users or receivers can be located in either the far-field or the near-field region of an RIS. The authors of [14], [15] derive closed-form expressions for computing the intensity of the electric field (E-field) in two asymptotic regimes that are representative of the far-field and near-field regions of an RIS. They also characterize the scaling laws of the EM field scattered by an RIS as a function of its size, the transmission distances, and the wave transformations.

Similarly, an RIS may be located in either the far-field or the near-field of a transmitter/source. If the RIS is located in the far-field of a source, the EM waves appear as plane waves to the RIS, and the source is referred to as a planewave source. On the other hand, if the RIS is located in the near-field of a source, the EM waves appear as spherical waves to the RIS, and the source is referred to as a point source for simplicity. Therefore, as shown in Figure 2, in RIS-assisted wireless communications, four cases can emerge depending on the source type and receiver location from the RIS.

1) *Case 1:* The transmitter appears as a *point source* to the RIS, and the receiver is located in the *far-field* of the RIS.
2) *Case 2:* The transmitter appears as a *planewave source* to the RIS, and the receiver is located in the *far-field* of the RIS.
3) *Case 3:* The transmitter appears as a *point source* to the RIS, and the receiver is located in the *near-field* of the RIS.
4) *Case 4:* The transmitter appears as a *planewave source* to the RIS, and the receiver is located in the *near-field* of the RIS.

In this paper, we only consider cases 1 and 2, where the receiver is located in the far-field of the RIS. It is well known

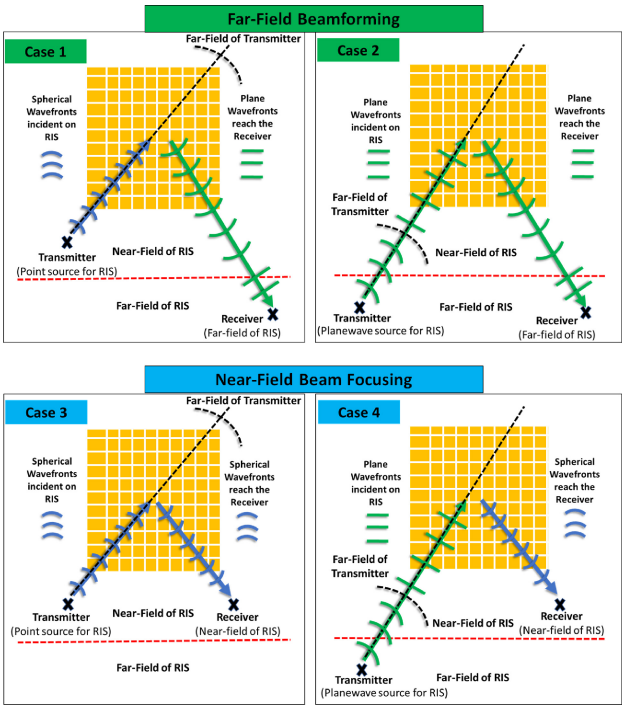

FIGURE 2. RIS-assisted wireless communication: Four cases depending upon transmitter and receiver location relative to the RIS.

in the literature that due to the product-distance path loss model of RIS-assisted communications in the far-field, the RIS should ideally be placed closer to either the transmitter or the receiver [11]. In cases 1 and 2, the RIS is assumed to be located far from the receiver (far-field beamforming cases). In case 1, the RIS is located closer to the transmitter, while in case 2, it is located far from the transmitter. Analytical and computational techniques to determine the radiation patterns are also simplified for the far-field beamforming cases because the elevation and azimuth angles from every unit cell of the RIS to the receiver are approximately the same [16]. Cases 3 and 4 are also interesting. However, implementing them in full-wave EM simulators for multiple designs is more time-consuming, and their inclusion in the current paper will double the results without adding much insight. Therefore, we exclude them from this paper and leave them as future work.

Various authors have investigated the theoretical gains of RIS in different cases. Such studies are reviewed in [11]. It is important to highlight that in the context of wireless communications, most of these papers are not concerned with optimizing complete radiation patterns created by the RIS. Instead, they typically optimize a utility function at a particular location of one or more receivers. However, the radiated beams towards undesired directions cannot be ignored for practical RIS. The authors of [17], used an analytical path loss model for computing the power observed at a given location of an RIS-assisted communication link and developed an algorithm for investigating the unwanted beams created by different designs. The desired reflection angles were set to 45 and 75 degrees (single beam steering), but almost all the considered designs produced significant powers at numerous unwanted angles. Therefore, during the optimization of RIS and selection of unit-cell design, it is important that the entire radiation patterns are considered.

RIS is a nearly-passive device because its unit cells do not amplify the incident EM waves. However, power is still required to change unit cells' states to achieve reconfigurability. Generally, a unit cell design with more PIN-diodes (more states) provides better reconfigurability but requires more power. In this context, exploring the trade-offs between unit cell design, surface-level radiation pattern generation capabilities, power requirements, and control circuit complexity is also important.

A. MOTIVATION

A wide variety of unit cell designs that can be used to fabricate an RIS is available in the literature. Proposing new unit cell designs is also an active area of research. In future wireless network deployments, RIS is expected to be used mostly for single beam steering or multi-beam forming with equal/unequal power levels at different angles. Such RIS will be required to produce a set of useful radiation patterns routinely. Unfortunately, there is a lack of standardized benchmarks, such as a set of full radiation patterns, to evaluate and compare the performance of RIS made of different unit cells. Moreover, various authors assume different numbers of unit cells and inter-cell spacing on their surfaces. Such differences make it challenging to fairly compare the relative performance of different designs in generating some surface-level full radiation patterns. To fill this gap, in this paper, we introduce a framework that consists of eight full radiation patterns as benchmarks, including two having single beams and six having two to eight beams at different angles. The framework allows us to fairly compare different designs and then select the best one according to the required NLOS application.

A significant difficulty also lies in finding the states of the PIN diodes of each unit cell to achieve some desired radiation response. The search space has exponential complexity, and the problem is NP-hard [18] even for a moderately sized RIS comprising 20 to 30 unit cells. While efficient algorithms exist to determine the states of the PIN diodes, they primarily target wireless communications and rely on simplistic models. Data rates at specific locations are their primary design objective rather than the entire radiation pattern. Thus, these algorithms do not account for how an RIS reflects signals in unwanted directions during the design stage. It is crucial to acknowledge that even the most efficient algorithms may not succeed if a finite-sized RIS created from a given unit cell design cannot generate an untested radiation pattern. These difficulties motivate the need for full radiation patterns that can act as benchmarks to test and compare the performance of various designs.

B. PROPOSED APPROACH AND CONTRIBUTIONS

In this paper, we introduce a benchmarking framework and metrics that can be used to assess the radiation pattern generation capabilities, power requirements, and control circuit complexity of RISs fabricated from various unit cell designs, specifically those employing PIN diodes for tuning, under point/planewave source assumptions for far-field beamforming. We also explore trading the radiation pattern generation capability for control circuit complexity through unit cell grouping. To achieve our goal, we establish a set of radiation patterns, both simple and complex, as benchmarks within our framework.

To evaluate the effectiveness of our proposed benchmarking framework and to analyze the tradeoffs, we consider five different unit cell designs from the literature. Using full-wave simulations, we compare the performance of five finite-sized RIS constructed from each unit cell design [18], [19], [20], [21]. Three designs utilize 1-bit control achieved through a single PIN diode, while the remaining two utilize 2-bit control via multiple PIN diodes. Four of these designs (two 1-bit and two 2-bit) are optimized to generate the maximum phase differences between different diode states, i.e., 180° for 1-bit and 90° for 2-bit designs. The fifth design (1-bit) is unoptimized and gives only a 50° phase shift between its two diode states. The unoptimized unit cell design allows us to understand the role of unit cell optimization in producing desired surface-level radiation patterns. At normal incidence, all the designs in our study exhibit reflection coefficients between 0.85 and 1.0.

Numerical experiments are conducted to assess the ability of the considered RISs to replicate the benchmarking patterns in the far-field, assuming a normal angle of incidence for incoming EM waves using point/planewave source assumptions. To compare the relative performance of various designs, we introduce three useful metrics, which are the directivity error (DE), normalized mean squared error (NMSE), and side lobe ratio (SLR). We also analyze the complexity of the control circuit and the power requirements for each design. We also discuss controlling unit cells in groups and evaluate the tradeoff between the radiation generation capabilities and control circuit complexity. Our key findings are summarized below.

- When assuming a point source (case 1), we observe that an RIS made from a 1-bit unit cell design outperforms an RIS made from a 2-bit design. The control circuit complexity and power requirements of 1-bit unit cell designs are also less than the 2-bit designs. The improved performance mainly results from the spherical curvature of the wavefronts and is consistent with the results in the literature [22].
- In the case of a planewave source (case 2), an RIS made from a 1-bit unit cell design exhibits significantly poorer beam steering performance than an RIS made from a 2-bit unit cell design.
- When the unit cells on an RIS are controlled in groups, the performance of poor designs is less affected, which also reveals that making large surfaces out of poor designs would hardly improve surface-level performance.
- If a simple radiation pattern, such as a single beam steering at small reflection angles (less than 40°), is required, unoptimized unit cell designs may also be used.
- RISs are nearly-passive devices as they do not add new power to the incoming radio signals, but the power requirements of the control circuit cannot be ignored.

We believe that the benchmarking framework and performance metrics proposed in the present paper are extremely useful in studying the interplay between the unit cell and surface-level RIS design. Our proposed approach can help select appropriate designs for future RIS-assisted wireless communication systems in urban environments.

The rest of the paper is organized as follows. In Section II, we discuss the unit cell designs and the E-field produced by RIS; in Section III, we discuss the RIS control circuit and analyze its complexity and power requirements; in Section IV, we present the benchmarking framework and performance metrics; in Section V, we present the simulation results; and in Section VI, we conclude the paper.

II. UNIT CELL AND RIS

A. UNIT CELL—THE BASIC ELEMENT OF RIS

RIS designs can be classified in multiple ways. One such classification is discrete vs. continuous RIS. In a discrete RIS, a microstructure called unit cell forms the basic building block. A finite number of unit cells are arranged in a rectangular array to obtain a discrete RIS. On the other hand, a continuous RIS can be thought of as a virtually uncountably infinite number of unit cells integrated into a limited surface area. In these designs, tunable circuits, such as PIN diodes or varactors, are used to dynamically change the surface impedance for controlling the incident EM waves. In continuous RIS, the impedance pattern is a map of the hologram and can be calculated directly from the field distribution of the provided reference wave and reflected object wave [23].

In this paper, we exclusively focus on discrete RISs that are made up of unit cells controlled by PIN diodes. In the rest of the discussion whenever we refer to a unit cell, we will refer to a discrete design with PIN diodes as control elements. The unit cell size depends on the frequency of operation, with higher frequencies requiring smaller dimensions. The total number of unit cells in a fixed-size RIS depends on its shape and size. By joining multiple smaller surfaces with repeating pattern of unit cells, large-sized RISs can be made. It is important to note that we define RIS as a repeating pattern of unit cells jointly controlled either with a single controller or a set of controllers.

A category of RIS research focuses entirely on unit cell design and its EM properties. Various unit cell designs are available in the literature. Usually, a design that employs

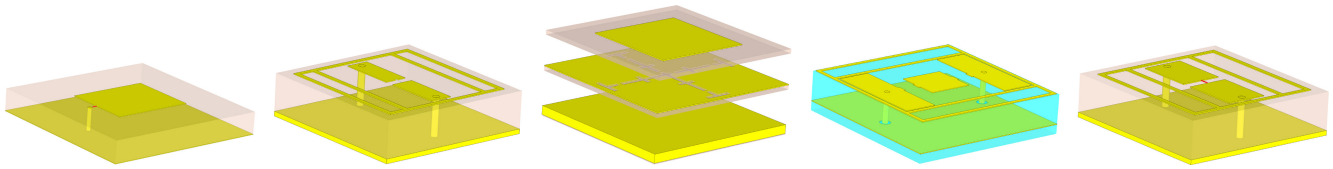

FIGURE 3. (from left to right) Unit cell layouts of S_1 [18], S_2 [19], S_3 [20], S_4 [21], S_5 [19].

TABLE 1. Control circuit complexity and maximum power requirements of RIS S_1-S_5 each made from MN unit cells. $P_D = 8mW$.

RIS	n	d	RIS Control Circuit Complexity		Maximum RIS Power Requirements					
			RIS Physical Control Circuit Paths	RIS Function Switching Rate	RIS Total Power ($dMNP_D$)	unit cell Dimensions (mm)	Unit Cell Area $\times 10^{-4}$ (m^2)	Reflection Coefficient at normal incidence angle (magnitude$\angle$phase°)	f (GHz)	RIS Power Per Unit Area (W/m^2)
S_1 [18]	1	1	MN/G	$GK/(MN\tau)$	MNP_D	5.8×4.9	1.82	$0.95\angle_1 0°$, $0.92\angle_2 180°$	11.1	44
S_2 [19]	1	1	MN/G	$GK/(MN\tau)$	MNP_D	6×6	2.89	$0.90\angle_1 0°$, $0.88\angle_2 180°$	8.82	27.7
S_3 [20]	2	5	$2MN/G$	$GK/(2MN\tau)$	$5MNP_D$	50×50	42.3	$0.95\angle_1 0°$, $0.95\angle_2 90°$, $0.98\angle_3 180°$, $0.92\angle_4 270°$	2.3	9.46
S_4 [21]	2	2	$2MN/G$	$GK/(2MN\tau)$	$2MNP_D$	8.8×8.8	2.72	$0.88\angle_1 0°$, $0.85\angle_2 90°$, $0.92\angle_3 180°$, $0.90\angle_4 270°$	9.08	58.8
S_5 [19]	1	1	MN/G	$GK/(MN\tau)$	MNP_D	6×6	6.25	$0.92\angle_1 0°$, $0.94\angle_2 50°$	6.00	12.8

a single PIN diode can produce two phases (1-bit control), while a design that uses at least two PIN diodes can produce four distinct phases (2-bit control). There are very few PIN diode based unit cell designs in the literature that produce eight or more distinct phases (designing such unit cells is challenging) [24], [25]. Another important consideration while designing a new unit cell is the phase shifts that are obtained when the PIN diodes are in their different states. Ideally, the resulting phases should be maximally apart, i.e., 180° in the case of 1-bit unit cell designs and 90° in the case of 2-bit unit cell designs. Unit cell designs that produce maximally apart phase shifts will be referred to as optimized designs. In general, the amplitude of the reflection coefficient is preferable to be one to maximize the radiation efficiency. In practice, this is never the case and also there is a strong correlation between the phase and amplitude of the reflection coefficient of the unit cell.

Keeping all of these factors into consideration, we select five designs from the literature. The layouts of the considered unit cells are shown in Figure 3. The unit cell design proposed in [18] has a sandwich structure composed of a simple rectangular patch, a metal ground plane, and a single PIN diode that connects one edge of the patch to the ground through a metallic via. The authors of [19], propose a three-layer unit cell design, which is again controlled through a single PIN diode. A relatively more complex unit cell is proposed in [20]. This design consists of 5 PIN diodes, but only two control signals are required; therefore, we can classify this as a 2-bit design. Four configurations of 5 PIN diodes produce four almost 90° apart phase shifts. The unit cell is symmetric but has a relatively complex structure and consists of an upper patch, a slot-loaded plane, and a ground. Another 2-bit unit cell design using only 2 PIN diodes is proposed in [21].

We denote the RISs made from the unit cell designs proposed in [18], [19], [20], [21] as S_1, S_2, S_3, and S_4 respectively. Along with these four optimized designs, we also consider an unoptimized unit cell design. The unoptimized design is obtained by modifying [19], and we refer to it as S_5. This design can only produce a phase shift of 50° between its two configurations, allowing for testing the necessity and extent of unit cell optimization for achieving good performance. Table 1 summarizes the design frequency, reflection amplitudes, and phases of all these unit cells in different control states at a normal incidence angle.

Please note that in this paper, we only consider those designs that reflect the signals. Recently some authors have also proposed omni-surfaces that are capable of reflection as well as refraction (transmission) to provide coverage to users who are located on the opposite side of the surface [26], [27]. In this case, the signal passes through the unit cell and then reaches the receiver located on its opposite side. The

consideration of such designs is beyond the scope of our work.

B. E-FIELD OF RIS

In an RIS-assisted communication system, the E-field at a receiver can be computed as

$$E(\theta_r, \phi_r) = \sum_{m=1}^{M}\sum_{n=1}^{N}\left[E_{mn}^{in} e^{j\alpha_{mn}} f\left(\theta_{mn}^{t}, \phi_{mn}^{t}\right) f\left(\theta_{mn}^{r}, \phi_{mn}^{r}\right) |\Gamma_{m,n}| e^{j\Phi_{mn}} e^{jk\cdot\hat{r}_{mn}}\right] \quad (1)$$

where, θ_r and ϕ_r are the elevation and azimuth angles from the center of the RIS to the receiver, $e^{jk\cdot\hat{r}_{mn}}$ represents the wave vector, E_{mn}^{in} and α_{mn} are the illuminating amplitude and phase, $f(\theta_{mn}^{t}, \phi_{mn}^{t})$ is the radiation response of the $(m,n)^{th}$ unit cell where the angles ϕ_{mn}^{t} and θ_{mn}^{t} are the elevation and azimuth angles from the $(m,n)^{th}$ unit cell to the transmitter, $f(\theta_{mn}^{r}, \phi_{mn}^{r})$ is the radiation response of the $(m,n)^{th}$ unit cell where the angles ϕ_{mn}^{r} and θ_{mn}^{r} are the elevation and azimuth angles from the $(m,n)^{th}$ unit cell to the receiver, and $\Gamma_{mn} = |\Gamma_{mn}|e^{j\Phi_{mn}}$ is the complex reflection coefficient of the $(m,n)^{th}$ unit cell, where $|\Gamma_{m,n}|$ is the magnitude and Φ_{mn} is the phase shift produced by the $(m,n)^{th}$ unit cell. The phase shifts imposed by the unit cells are controlled by changing the PIN diode states. The complex reflection coefficients of the five unit cell designs considered in this paper are given in Table 1. In (1), we have assumed omnidirectional transmit and receive antennas with unity radiation responses.

In the far-field beamforming scenario (both cases 1 and 2), $f(\theta_{mn}^{r}, \phi_{mn}^{r}) = f(\theta_r, \phi_r)$; $\forall m, n$. Furthermore, in case 2 under the planewave source assumption $f(\theta_{mn}^{t}, \phi_{mn}^{t}) = f(\theta_t, \phi_t)$; $\forall m, n$, where θ_t and ϕ_t are the elevation and azimuth angles from the center of the RIS to the transmitter, $E_{mn}^{in} = E$, $\forall m, n$, and $\alpha_{mn} = \alpha$, $\forall m, n$. If the unit cell radiation response has no azimuthal dependence then $f(\theta_r, \phi_r)$ and $f(\theta_t, \phi_t)$ further simplify to $f(\theta_r)$ and $f(\theta_t)$ respectively.

The radiation response of a unit cell is related to its specific design. In Figure 4, we show the normalized radiation responses with respect to the elevation angle θ of four optimized unit cells that are studied in this paper. These radiation responses are obtained using full-wave simulations. We also plot $f(\theta) = \cos^{\frac{1}{q}}(\theta)$ for certain values of q for comparison. The radiation response of the unit cells used in S_1 and S_3 is similar to $\cos^{\frac{1}{3}}(\theta)$, while that of S_2 and S_4 is similar to $\cos^{\frac{1}{5}}(\theta)$.

In the literature, we also find equivalent circuit modeling approaches for the characterization of unit cells and RIS [26], [28]. In these methods, appropriate impedances that model the reflection and refraction behavior are determined with the help of circuit and EM field theories. These analytical models are simple to use and greatly simplify the analysis at the expense of accuracy. In our paper, we do not use equivalent circuit models. Instead, the unit cell designs as given in the literature are replicated in CST, and at the surface level, we use array factor approximations.

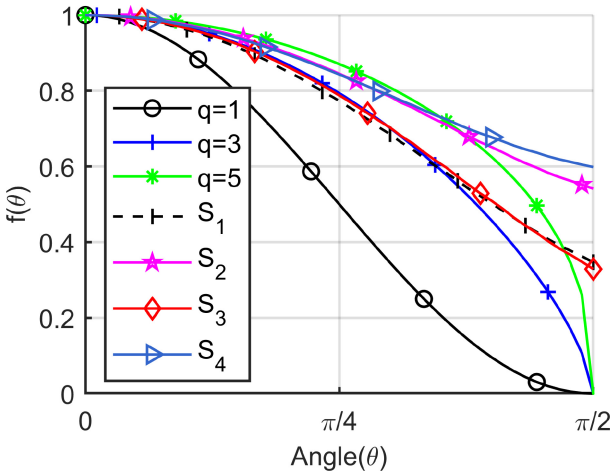

FIGURE 4. Normalized radiation response $f(\theta)$ of the four optimized unit cells used in S_1-S_4. The powers of $\cos^{\frac{1}{q}}(\theta)$ for $q = 1, 3, 5$ are also plotted.

III. CONTROL AND POWER REQUIREMENTS OF RIS

This section discusses the control circuit complexity and power requirements of RIS built from different unit cell designs. Table 1 summarizes the control circuit complexity, power requirements, and unit area power requirements of RIS S_1-S_5.

A. PHYSICAL AND LOGICAL CONTROL PATHS ON RIS

Each unit cell incorporates PIN diodes and therefore requires independent control signals. For an n-bit unit cell, n separate control lines are required, and 2^n distinct phases can be generated. It should be noted that the total number of PIN diodes in an n-bit unit cell may exceed n, as in the case of [20], where five PIN diodes are used to produce four distinct phase shifts with only two control signals. The control signals are generated by a micro-controller or FPGA, which requires an additional interface circuit. However, these controllers have a limited number of pins, which may not be sufficient to control all the unit cells on a large RIS simultaneously. To address this issue, time division multiplexing is typically used, and this type of control architecture is referred to as active matrix architecture or I/O expansion [29].

Compared to varactor diodes, control circuits made of PIN diodes are more straightforward, and digital high and low states are sufficient for their ON/OFF control [30]. Additionally, PIN diodes have a much lower forward biasing voltage (0.7V–0.8V), but the forward-biased current is of the order of mA. Conversely, varactors operate at a significantly higher voltage than a digital high state of a PIN diode but require μA or less current when fabricated with the same technology [31]. As a result, varactors generally consume less power than PIN diodes. Nonetheless, PIN diodes are preferred because of their control simplicity.

The rate at which an RIS can switch between different functionalities (we refer to it as the RIS function switching) is directly dependent on the speed of the control circuit. In fast-changing wireless channels, the RIS function switching

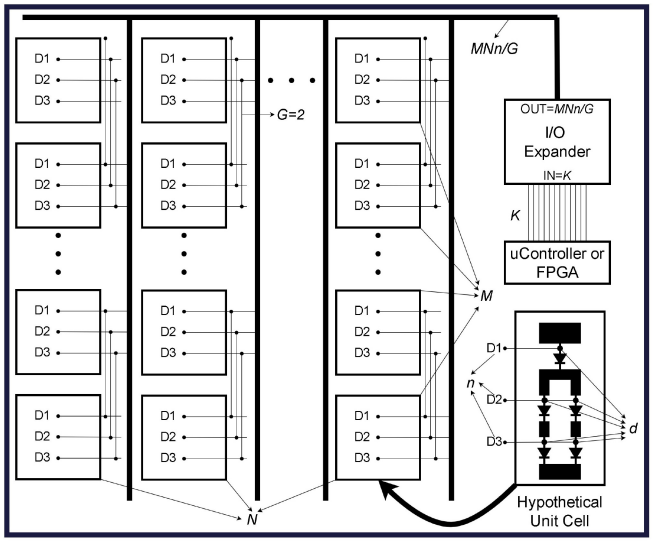

FIGURE 5. RIS control circuit, unit cell grouping, and I/O expansion for addressing.

must also be fast. However, the number of unit cells on the RIS affects the channel sensing overhead and the complexity of the control circuit. Fewer unit cells mean a lower channel sensing overhead and less complex control circuit, but it also affects the RIS ability to generate complex radiation patterns [32]. To reduce the channel sensing overhead and control circuit complexity, the unit cells can be grouped and controlled simultaneously. This also negatively impacts the RIS radiation pattern generation capabilities and overall functionality. To investigate the extent to which unit cell grouping affects the performance of RIS S1-S5, it is necessary to quantify these tradeoffs using the benchmarking framework and performance metrics discussed in the next section.

Using Figure 5, we illustrate the concept of unit cell grouping and distinguish between physical and logical control paths. The figure depicts groups of two unit cells, where each unit cell contains three PIN diodes labeled as D1, D2, and D3, enclosed within a rectangular box. The RIS comprises MN unit cells, with K micro-controller pins available for control purposes, where $K < MN$. The K pins drive control signals to the first K unit cells or groups of unit cells at the same time, while the remaining cells or groups are disabled. Then, the next K unit cells or groups of unit cells are enabled, and the same K pins provide new control signals. This sequence continues until all the unit cells or groups of unit cells have been addressed, leading to logically separated control paths. It is worth noting that increasing the number of controllers that operate in parallel increases the overall design cost but also allows for an increase in the total number of control pins.

The number of physical control circuit paths can be expressed as $\frac{MNn}{G}$, where G is the number of unit cells in each group. By increasing the value of G, the complexity of the control circuit can be significantly reduced. The order of the RIS function switching rate can be quantified as $O(\frac{GK}{MNn\tau})$, where τ represents the response time of the slowest element in the control path. For example, if we consider an RIS composed of 2-bit unit cells with $G = 2$, $M = N = 40$, $K = 40$, and $\tau = 20$ns, the function switching rate would be 1.25 MHz, enabling the RIS to switch from one radiation pattern to another in approximately 0.8μs. In the frequency range of 1 GHz to 30 GHz, the typical wireless channel coherence time varies from a few hundred μs to a few μs, which implies that the RIS can quickly adapt to changing wireless channel conditions. Additionally, several PIN diodes, including SMP1340, can operate at a GHz switching rate, which can make the RIS function switching even faster. However, the actual switching rate would depend on several factors, such as the channel sensing overhead and the power requirements of the switching circuitry. We can also observe a tradeoff between the number of physically independent control circuit paths and the function switching rate.

B. POWER REQUIREMENTS OF RIS CONTROL CIRCUIT

The power consumption of a PIN diode when in the ON state depends on its forward voltage drop and forward operating current. While the power consumption of a single PIN diode is relatively low, typically around 7-8mW [30], it becomes significant when multiple unit cells with multiple PIN diodes are combined to form large surfaces. It is challenging to determine the average percentage of unit cells that need to be forward-biased to achieve various functionalities. However, we know that the power requirements of an RIS are directly proportional to the number of PIN diodes on its surface. The proportionality constant is the ratio of PIN diodes in the ON state to the total number of PIN diodes. To simplify and facilitate comparisons, we assume that this proportionality constant is equal to 1.[1]

The maximum power requirement of an RIS made consisting of MN unit cells is $dMNP_D$, where P_D is the power used by one PIN diode when forward-biased (in the ON state). It is apparent that a unit cell configuration where $d > n$ is less efficient than one where $d = n$. Additionally, as the value of n per unit cell increases, so does the power requirement. The impact of grouping the unit cells on power usage would rely on the diode states for each group. For instance, if we take the 1-bit unit cell design, all of the unit cells in a group would be ON if they received an ON signal. Conversely, if they receive an OFF signal, all of them would be OFF. The maximum power requirements, on average, would remain the same. However, grouping simplifies the control circuit since all of the unit cells in a group will be in the same state, based on a single control signal.

Supplying power continuously to an RIS that consists of several hundred unit cells operating at very high frequencies

1. In reality, the proportionality constant should be less than 1 because only a fraction of diodes would be in the ON state for producing typical radiation patterns.

can pose a challenge. The power consumption of RIS per unit area (W/m^2) is a crucial factor to consider. In Table 1 we have computed these requirements for RIS S_1-S_5, assuming that the unit cells are arranged uniformly half wavelength apart. The table also presents the unit cell dimensions and design frequencies. For example, RIS-S_1 operates at a frequency of 11.1 GHz, and its power consumption per unit area is $44W/m^2$. Suppose we want to use solar panels that produce between 100-$200W/m^2$ during the sunshine hours. With this assumption, the size of solar panels required to power up RIS-S_1 is less than the size of the RIS. However, these observations quickly change when we consider higher frequencies (above 30 GHz), because the unit cell dimensions become small, and the size of solar panels required to power up the resulting RIS becomes greater than the RIS size itself.

IV. BENCHMARKING FRAMEWORK - RIS RADIATION PATTERNS AND PERFORMANCE METRICS

In a smart city environment where NLOS situations dominate, we expect RISs to possess three significant functionalities. These are single beam steering and multi-beam forming with equal power/unequal power levels at different angles. In the following subsection, we propose a flexible benchmarking framework that allows us to test these beamforming capabilities for RISs made from different unit cell designs under point/planewave source assumptions (cases 1 and 2).

A. BENCHMARK RADIATION PATTERNS

As benchmarks, we determine a set of typical radiation patterns based on NLOS scenarios. The considered set includes eight radiation patterns, which are shown in the first column of Figure 6. These radiation patterns are labeled as B_1-B_8 for referencing. Radiation patterns B_1 and B_2 are used to test the beam steering capabilities of RIS in a single direction. Radiation patterns B_3 (2 beams), B_4 (3 beams), B_5 (4 beams), B_6 (4 beams), and B_7 (8 beams) are used to test multi beamforming capabilities with equal power. Radiation pattern B_8 is used to test the formation of multiple unequal power beams (4 beams). The relative angles of various beams in these radiation patterns are shown in Figure 6. These patterns are referred to as the benchmarking patterns in further discussion. The prominent beams in these benchmarking patterns will be referred to as the main lobes. The side lobes in all the benchmarking patterns are desired to be negligible. In our study, the polarization of the incident EM wave and the operating frequency are assumed to match the design assumptions of each unit cell in the original papers. Our proposed framework is flexible, and more radiation patterns can be included in the benchmarking set depending on the application scenarios.

B. PERFORMANCE METRICS

We are interested in quantifying the relative ability of different RISs to reproduce the benchmarking patterns. To this end, appropriate metrics that can compare two radiation patterns are required. In this discussion, we will use the terms 'achieved radiation pattern' and 'reference radiation pattern,' where achieved radiation pattern means the pattern produced by the RIS in response to a given reference radiation pattern. We develop three performance metrics. The first metric is DE which measures the ability of RIS to reproduce the main lobes of the reference radiation pattern. The second metric is NMSE which quantifies the accumulative mean square error between the achieved and the reference radiation patterns in all directions. The third metric is SLR which quantifies the main lobe to the side lobe where the location of the main lobe is determined from the reference radiation pattern. Please note that our DE, NMSE, and SLR are comparative metrics, i.e., we use them to check how closely the achieved radiation pattern matches a reference radiation pattern. Below we further explain these metrics.

DE: We define DE as

$$\mathrm{DE} = \frac{D_r - D_a}{D_r} \tag{2}$$

where, D_r is the reference directivity that is determined by integrating the power (square of E-field) over the beam-width of the main lobe in the reference radiation pattern, while D_a is the achieved directivity that is determined by integrating the power over the starting and ending angles obtained from the beam-width of the main lobe of the reference radiation pattern in the achieved radiation pattern. We calculate the beam-width of the main lobe using the First Null Beam-Width (FNBW) criteria. In both D_r and D_a, the starting and ending angles of the main lobe of the reference radiation pattern are used because the objective is to reproduce the main lobe of the reference pattern. The value of DE is positive if the achieved radiation pattern is inferior to the target radiation pattern. Due to the normalization by D_r, the maximum positive value of DE is 1. A value of DE closer to 1 indicates that the main lobes are not formed in the intended directions and are in completely different directions (inferior performance). The value of DE becomes negative if the achieved radiation pattern is better than the target radiation pattern (this is possible if the benchmarking pattern is not used as a reference radiation pattern).

NMSE: The NMSE is computed as

$$\mathrm{NMSE} = \frac{1}{L}\sum_{\theta,\phi}\left(\frac{E_r(\theta,\phi)}{E_{rmax}} - \frac{E_a(\theta,\phi)}{E_{amax}}\right)^2 \tag{3}$$

where, $E_r(\theta,\phi)$ is the E-field of the reference radiation pattern and $E_a(\theta,\phi)$ is the E-field of the achieved radiation pattern at the elevation and azimuth angles θ and ϕ. We normalize the E-field of each radiation pattern by the corresponding maximum values, i.e., E_{rmax} for the reference radiation pattern and E_{amax} for the achieved radiation pattern. We then average the squared difference of the normalized E-field values in all the directions to obtain NMSE. In the simulations, we use $L = 180 \times 360$.

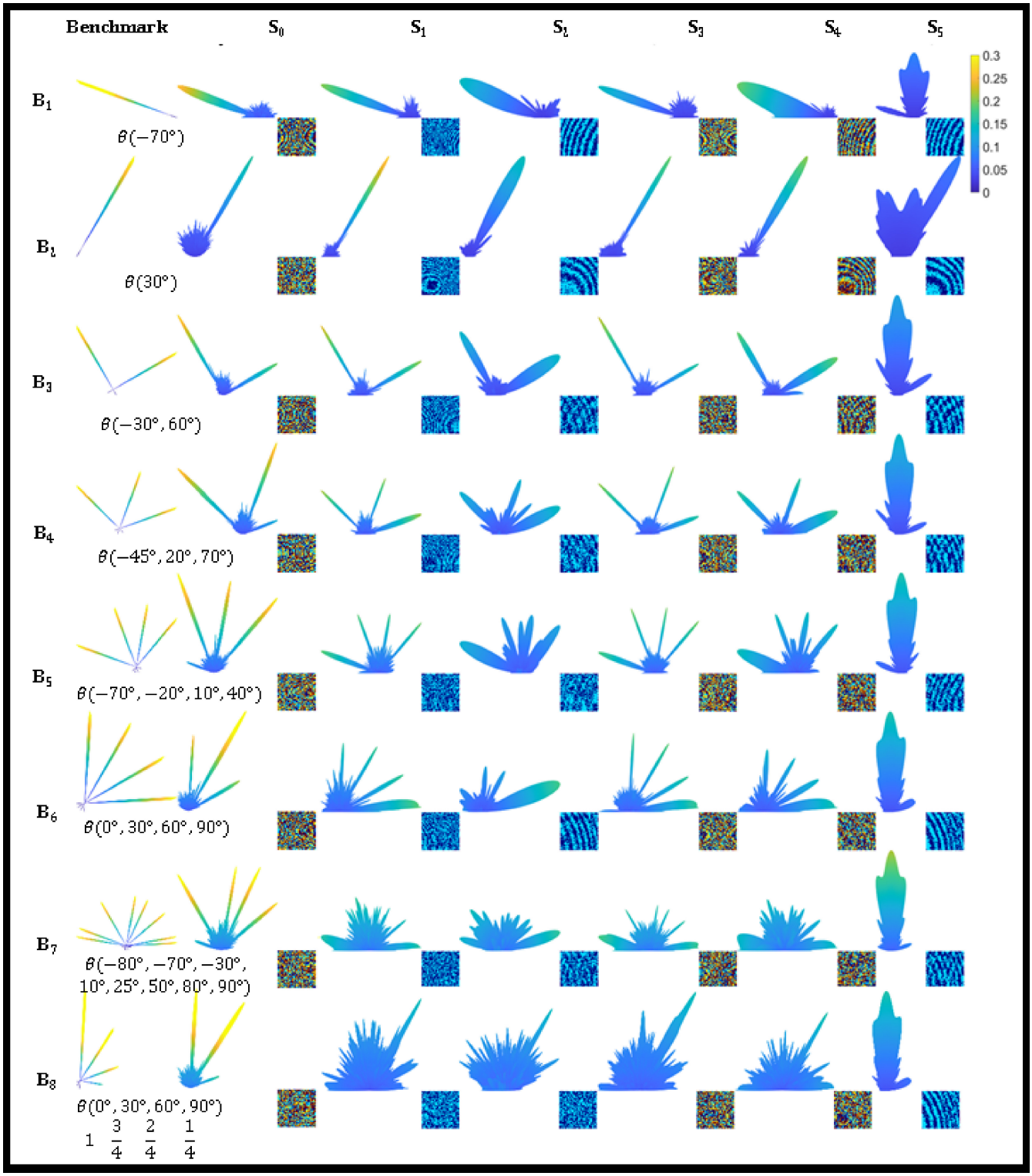

FIGURE 6. Benchmarking radiation patterns B_1-B_8 and the radiation patterns obtained by RIS S_1-S_5 under point source assumptions (case 1) without unit cell grouping ($G = 1$). The results for the reference RIS S_0 are also shown. The RIS configuration matrix (40 × 40) is also reported as a colored image (unit cell state 1=Blue, 2=Cyan, 3=Yellow, 4=Red). The elevation identifies beam directions (θ, ranges between 0° and 90°) and azimuth (ϕ, only takes two values 0° and 180°) angles. Instead of repeating the two ϕ values, θ and $-\theta$ are used ($-\theta = \theta_{\phi=180°}$).

SLR: SLR is computed in dB scale

$$\text{SLR} = 10\log_{10}\frac{\text{Power density of intended lobe}}{\text{Power density of side lobe}} \quad (4)$$

We determine the location of the intended lobe (starting and ending angles) from the reference radiation pattern. At these angles, we look for the power density in the achieved

TABLE 2. Quantitative results of five RIS $S_1 - S_5$, with and without unit cell grouping under point source assumptions with the observer in the far-field (case 1). Best values (smallest in case of DE and NMSE and largest in case of SLR) are highlighted in bold font, worst values (largest in case of DE and NMSE and smallest in case of SLR) are highlighted in *italic* font.

ID	Grouping	Relative Directivity Error (DE)					Relative Normalized Mean Squared Error (NMSE)					Side Lobe Ratio (SLR) - dB				
		S_1	S_2	S_3	S_4	S_5	S_1	S_2	S_3	S_4	S_5	S_1	S_2	S_3	S_4	S_5
B_1	No ($G = 1$)	0.5	0.39	**0.16**	*1*	0.94	0.1004	*0.1248*	0.091	0.1131	**0.0889**	11.58	9.02	8.69	**12.62**	*-1.11*
B_2		0.3	0.54	0.7	**0.24**	*0.82*	**0.0284**	0.0459	0.0381	0.0311	*0.0516*	9.96	11.01	8.86	**11.62**	*6.27*
B_3		0.22	0.29	0.47	**0.18**	*0.91*	**0.0757**	0.0774	*0.0919*	0.0852	0.0808	8.14	8.35	**8.86**	8.58	*-0.55*
B_4		**0.14**	**0.14**	0.19	0.16	*1*	0.1277	0.1382	0.1288	**0.1143**	*0.1412*	**9.21**	2.63	7.34	9.17	*-2.79*
B_5		0.07	0.39	**0.01**	0.04	*1*	0.1467	0.1569	**0.1414**	0.1427	*0.1812*	5.19	1.77	**5.65**	4.24	*-2.54*
B_6		0.15	0.53	**0.07**	0.26	*1*	0.137	0.1659	**0.1339**	0.1359	*0.1826*	5.16	**5.78**	3.63	3.41	*-0.71*
B_7		**0.16**	0.32	**0.16**	0.22	*1*	**0.1995**	0.2358	0.2136	0.2255	*0.305*	-0.65	-1.73	-0.26	**0.91**	*-7.26*
B_8		0.06	0.42	**0.01**	0.24	*0.79*	0.1634	0.1547	0.1623	**0.143**	*0.1657*	*-4.44*	-4.41	**2.22**	-3.96	-0.71
B_1	Yes ($G = 2$)	0.41	0.2	*1*	**0.14**	0.83	0.1071	*0.1139*	0.0961	**0.0952**	0.101	**10.09**	4.83	-9.79	9.67	*-14.68*
B_2		*1*	**0.67**	*1*	0.8	0.8	0.0627	0.059	*0.0722*	**0.0528**	0.0568	6.78	2.87	-2	**7.73**	*-7.72*
B_3		0.78	**0.49**	*1*	0.65	0.85	0.0847	**0.0813**	*0.1005*	0.0953	0.0896	3.54	3.18	-4.35	**7.32**	*-11.82*
B_4		0.97	0.74	*1*	0.73	**0.69**	0.1443	0.1296	0.1298	**0.1082**	*0.1582*	0.26	0.68	-1.19	**3.29**	*-12.43*
B_5		0.97	0.74	*1*	**0.7**	*1*	0.158	0.16	**0.1522**	0.1552	*0.1982*	**0.93**	-1.69	-6.41	0.07	*-13.54*
B_6		0.8	0.71	*1*	0.64	**0.26**	0.1606	0.1673	**0.145**	0.1525	*0.1836*	0.34	-2.08	-3.27	**3.21**	*-4.23*
B_7		*1*	**0.14**	*1*	0.56	0.7	0.2252	**0.2116**	0.2135	0.2137	*0.3168*	**-2.33**	-3.48	-3.89	-4.42	*-12.38*
B_8		0.93	**0.61**	*1*	0.63	*1*	0.1928	0.1871	*0.2205*	**0.1628**	0.1822	*-7.62*	-3.92	**-1.25**	-5.22	-0.77

radiation pattern. On the other hand, we determine the side lobe exclusively from the achieved radiation pattern of the RIS and define it as the most prominent non-intended minor lobe. We use the words 'intended' because these metrics aim to measure how faithfully a reference radiation pattern is reproduced. In the considered set, we also have some multi-beam ($B_3 - B_8$) reference radiation patterns. For such patterns, we individually compute the SLR for each intended beam according to (4) and then report their average.

The benchmarking patterns in the considered set are ideal, with negligible non-intended lobes. Therefore, considering the benchmarking patterns as reference radiation patterns for the computation of the quantitative metrics is not an effective way to analyze the relative performance of S_1-S_5. To avoid this problem, we consider a reference RIS that is referred to as S_0. We then compute the quantitative metrics with respect to the radiation patterns achieved by S_0. For all the comparisons, the starting and ending angles of the main lobes will always be those given in the benchmarking patterns. With this approach, negative values of DE will indicate that the performance of the given RIS in producing the beams in the intended directions, as shown in the benchmarking pattern, is better than that of S_0.

V. BENCHMARK-BASED EVALUATION RESULTS

In this section, we test the ability of RISs S_1-S_5 in reproducing B_1-B_8. The reference RIS S_0 is made from a perfectly optimized reference 2-bit unit cell whose normalized radiation response $f(\theta)$ is $\cos(\theta)$ [33], [34]. This response is plotted in Figure 4 and is denoted as $q = 1$ curve. Each RIS (including S_0) has 40x40 (1600) unit cells. A commercially available full-wave EM solver (CST) is used for unit cell simulations to obtain their exact radiation responses. We use the lumped element model (s-parameters) of PIN diodes from Skyworks SMP1340-040LF. We use the unit cell data from CST and array factor approximation to simulate the RIS radiation patterns under point/planewave source assumptions. A genetic algorithm (GA) implemented in MATLAB determines the optimal configurations (diode ON/OFF states) of the unit cells on each RIS for a given benchmarking pattern. Finite size RISs with discrete phase controls may fail to generate the desired radiation patterns exactly. Therefore, in our simulations, we stop the GA after 350 generations because we observe that there is no significant improvement even if we allow the algorithm to run longer. When the GA stops, we take the best match. We use the patterns produced by S_0 as reference radiation patterns for computing DE, NMSE, and SLR metrics.

A. CASE 1: POINT SOURCE

The qualitative and quantitative results under point source assumptions are presented in Figure 6 and Table 2. The impact of unit cell grouping to reduce the control circuit complexity is also shown in Table 2.

1) PERFORMANCE WITH $G = 1$: WITHOUT UNIT CELL GROUPING

In Figure 6, we present the visual results that show the quality of the reproduced radiation patterns by each RIS

when we individually control the unit cells. The performance of S_0 is also plotted.

RIS - S_1: The visual quality of B_1-B_6 looks excellent, while that of B_7 and B_8 is poor. There are a few undesired main lobes in B_6, B_7 and B_8 as well as several high power side lobes, especially in B_8. However, the value of DE for B_8 is very small. The observations about the excellent quality of radiation patterns are confirmed by the corresponding numerical values of DE, NMSE, and SLR in each case, which are either the best or very close to the best values.

RIS - S_2: The visual quality of the radiation patterns produced by S_2 looks somewhat poorer than that produced by S_1. From Table 2, we find out that DE (except for B_1) and SLR (except for B_6, B_8) values are poor compared to S_1 on almost all the benchmarks. From Table 1, the control circuit complexity and power requirements of both S_1 and S_2 are the same. Therefore, between the optimized 1-bit RISs, S_1 performs better than S_2 on nearly all the performance metrics under the point source assumption with $G = 1$.

RIS - S_3: The visual quality of B_1-B_6 produced by S_3 is either similar or better than S_1 on more complex benchmarks. The quality of B_6-B_8 looks significantly better than S_1 and S_2. The quantitative metrics are also better for several benchmarking patterns. From Table 1, the control circuit complexity of S_3 is doubled while its function switching rate is halved compared with S_1 and S_2. Since S_3 is designed to operate in the S-band, the per unit area power requirements are significantly less than S_1 and S_2. However, the total power requirements of S_3 are the highest among all the RIS because each unit cell has 5 PIN diodes.

RIS - S_4: The visual quality of B_2-B_6 produced by S_4 is similar to S_1, S_2 and S_3. The quality of B_1-B_8 looks worse than S_3 and S_1 but better than S_2. We notice that DE is not significantly poor, but the performance is effectively degraded due to higher side lobes and scattering. The control circuit complexity and power requirements of S_4 are doubled than both S_1 and S_2. However, this RIS uses only 2 PIN diodes per unit cell, which significantly reduces its power requirements compared to S_3.

RIS - S_5: This surface is made of a 1-bit unoptimized unit cell. The visual quality of all the benchmarks is worse than all other RIS. However, on B_2, the main lobes are visible with one lobe along the desired direction along with two high-power side lobes. The visual quality on B_1-B_8 is inferior because there is no correlation between the radiation pattern produced by S_5 and the target radiation pattern. S_5 is incapable of steering even a single beam at significantly large reflection angles. The control circuit complexity and power requirements of S_5 are similar to those of S_1 and S_2.

In terms of reproducing B_1-B_8 under the point source assumptions with $G = 1$, the overall performance of S_3 is the best, followed by S_1, S_4, S_2 and S_5. However, when we also consider the control circuit complexity and power requirements along with the DE, NMSE, and SLR, S_1 seems to be an overall better choice. However, in application scenarios where B_6-B_8 are mostly required, S_3 should be preferred despite its complexity and power requirements. Finally, if the application scenario only demands beam steering at smaller angles (such as B_2), then S_5 or its slightly more optimized version may also be used.

2) PERFORMANCE WITH $G = 2$: WITH UNIT CELL GROUPING

We now evaluate the performance of RIS S_1-S_5 assuming that the unit cells are grouped into pairs. This way, the RIS complexity, and sensing overhead are halved. However, the maximum power requirements remain unchanged. The resulting impact due to unit cell grouping on the ability of different RISs to produce the benchmarking patterns is quantified in the lower half of Table 2. We can see that the performance of all the designs is reduced. However, the extent of degradation for each design is different.

With $G = 2$, the best performance is shown by S_2 followed by S_4, S_1, S_5 and S_3. We again highlight that the DE value of 1 means that the surface has failed to produce the main beams in the intended directions. Poor performing RISs without grouping (S_2, S_4 S_5) are least affected by unit cell grouping and therefore we expect small gains in their performance even if we further increase their size. On the other hand, the gains in the performance of S_1 and S_3 become significantly higher with the corresponding increase in the RIS size. Meanwhile, the choice of beam steering angles and the variation in beam power levels significantly raise the required performance criteria for RIS designers as we witness in the case of B_8.

B. CASE 2: PLANEWAVE SOURCE

The qualitative and quantitative results under planewave source assumptions are presented in Figure 7 and Table 3. In this case, the number of unit cell control states greatly impacts the performance.

1) PERFORMANCE WITH $G = 1$: WITHOUT UNIT CELL GROUPING

The qualitative results without unit cell grouping ($G = 1$) are shown in Figure 7, while the corresponding quantitative results are presented in the upper half of Table 3.

RIS - S_1: We observe that the RIS can reproduce the main lobes, but there are non-intended side lobes in every radiation pattern produced by S_1. These side lobes are called 'quantization lobes.' They generally appear in RISs made from 1-bit unit cells due to more pronounced phase rounding quantization effects [35], [36]. The RIS can reproduce the main lobes, therefore, the DE values are very good in four out of eight benchmarking patterns (B_1-B_3, B_5). However, the NMSE is very bad compared to the best NMSE obtained for RIS S_4 in the same tests. The side lobe level of S_1 is close to 0 or negative in some cases, which shows that a significant amount of power is radiated in the unwanted directions.

RIS - S_2: This 1-bit RIS also produces quantization lobes. We observe that the main lobes are wider compared to S_1.

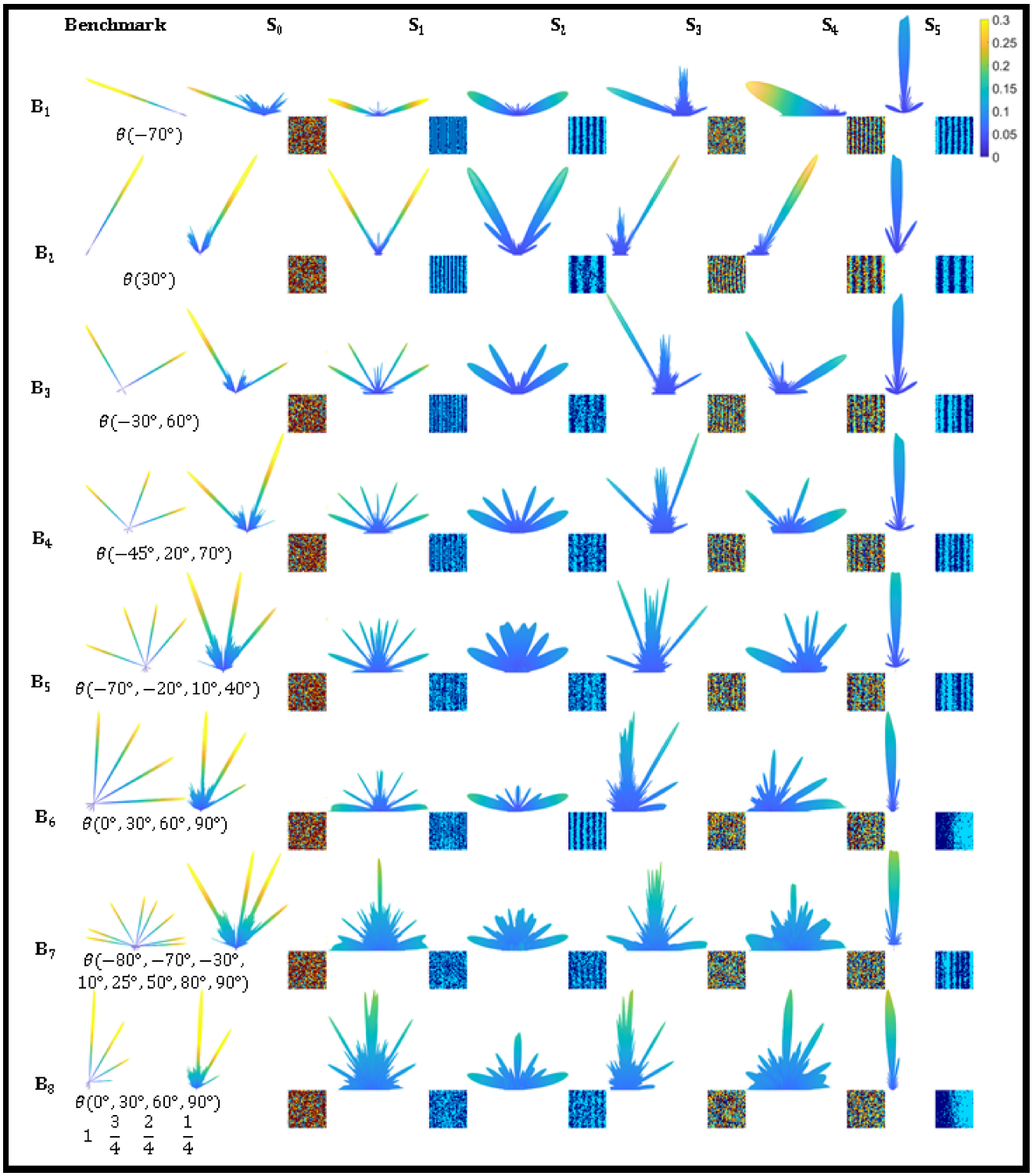

FIGURE 7. Benchmarking radiation patterns B_1-B_8 and the radiation patterns obtained by RIS S_1-S_5 under planewave source assumptions (case 2) without unit cell grouping ($G = 1$). The results for the reference RIS S_0 are also shown. The RIS configuration matrix (40 × 40) is also reported as a colored image (unit cell state 1=Blue, 2=Cyan, 3=Yellow, 4=Red). The elevation identifies beam directions (θ, ranges between 0° and 90°) and azimuth (ϕ, only takes two values 0° and 180°) angles. Instead of repeating the two ϕ values, θ and $-\theta$ are used ($-\theta = \theta_{\phi=180°}$).

On quantitative metrics, except for B_6, the performance of S_2 is generally poor, and the NMSE is very close to S_1 in all the tests. The side lobes are comparable to or even higher than the main lobes making the SLR values close to 0 or negative and again indicating a significant amount of power radiation in the unwanted directions.

TABLE 3. Quantitative results of five RIS $S_1 - S_5$, with and without unit cell grouping under planewave source assumptions with the observer in the far-field (case 2). Best values (smallest in case of DE and NMSE and largest in case of SLR) are highlighted in bold font, worst values (largest in case of DE and NMSE and smallest in case of SLR) are highlighted in *italic* font.

ID	Grouping	Relative Directivity Error (DE)					Relative Normalized Mean Squared Error (NMSE)					Side Lobe Ratio (SLR) - dB				
		S_1	S_2	S_3	S_4	S_5	S_1	S_2	S_3	S_4	S_5	S_1	S_2	S_3	S_4	S_5
B_1	No ($G = 1$)	**-0.13**	0.73	*1*	0.15	*1*	*0.0166*	0.0138	0.014	**0.0102**	0.0158	0.04	0.17	-8.51	**14.14**	*-14.03*
B_2		**0.12**	0.93	0.99	0.55	*1*	*0.01*	0.0092	0.0082	**0.0049**	0.0097	-0.03	0.05	-3.28	**10.2**	*-8.82*
B_3		**0.61**	0.89	0.98	0.8	*1*	0.0119	0.0112	0.0113	**0.0074**	*0.0129*	-0.09	0.02	-8.34	**6**	*-12.97*
B_4		0.78	0.91	*0.99*	**0.76**	*0.99*	0.0117	0.0116	0.0121	**0.0083**	*0.0141*	-0.17	-0.49	-9.84	**5.7**	*-16.3*
B_5		**0.86**	0.92	*0.93*	0.88	0.87	0.0139	0.0142	0.0158	**0.0112**	*0.0184*	-0.14	-3.38	-11.79	**0.98**	*-15.62*
B_6		0.6	**0.52**	0.84	0.75	*0.88*	0.0141	*0.0171*	0.0119	**0.0079**	0.0154	-1.58	-3.19	*-8.15*	**2.39**	-6.49
B_7		0.97	0.97	0.92	*0.98*	**-0.05**	0.0185	0.0184	0.0237	**0.018**	*0.0259*	-5.68	**-3.29**	-16.15	-4.74	*-20.78*
B_8		*1*	*1*	*1*	**0.99**	*1*	0.0131	0.0131	0.0148	**0.012**	*0.0171*	-4.72	3.58	-1.25	*-6.15*	**5.04**
B_1	Yes ($G = 2$)	0.16	0.74	*1*	**0.14**	0.98	0.1988	**0.1553**	*0.3117*	0.1762	0.2235	-0.19	-0.264	-1.958	**2.704**	*-3.088*
B_2		**0.13**	*1*	*1*	0.52	*1*	*0.2335*	0.1829	0.1096	**0.0317**	0.1279	-0.172	-0.276	-0.94	**1.936**	*-1.918*
B_3		**0.82**	*1*	*1*	*1*	*1*	0.1773	*0.2782*	0.2049	**0.0996**	0.2776	-0.308	-0.162	-1.926	**1.098**	*-2.77*
B_4		*1*	0.95	*1*	**0.85**	*1*	0.2178	**0.0701**	0.0887	0.1299	*0.3023*	-0.15	-0.266	-2.154	**0.918**	*-3.474*
B_5		*1*	*1*	0.99	*1*	**0.81**	0.1942	*0.2579*	0.2359	0.1888	**0.1287**	-0.292	-0.848	-2.578	**-0.018**	*-3.288*
B_6		0.72	**0.69**	*1*	0.87	0.96	0.2251	*0.3974*	0.1984	**0.0493**	0.129	-0.524	-0.738	*-1.734*	**0.232**	-1.404
B_7		0.94	*1*	*1*	0.94	**0.09**	0.2183	*0.3955*	**0.1911**	0.2659	0.3232	-1.328	**-0.926**	-3.334	-1.164	*-4.384*
B_8		*1*	**0.98**	*1*	*1*	*1*	**0.0649**	0.1213	0.2442	0.1574	*0.3597*	-1.236	0.424	-0.368	*-1.43*	**0.88**

RIS - S_3: There are no quantization lobes in the radiation patterns produced by S_3. The main lobes also look narrow and focused. However, the RIS fails to form the main lobes in the intended directions. The starting and ending angles of the main lobes in the benchmarking and the achieved radiation patterns are very close to each other, but there is no overlap due to narrow beams formed by S_3. Thus, the DE and SLR values are extremely poor because although beam steering is prominent it is not in the intended direction. On the other hand, the NMSE values are relatively good and the second best in the two cases (B_2 and B_3).

RIS - S_4: The visual quality of the radiation patterns produced by S_4 also looks good. There are also no quantization lobes in the reproduced patterns. The overall performance of S_4 is significantly better on all the benchmarks. This RIS can produce the main lobes with low side lobe levels. Moreover, the main lobes are wide as compared to S_3 and the starting and ending angles of the main lobes in the benchmarking and the achieved radiation patterns overlap. Therefore, the DE values are better than those for S_3 but relatively worse than S_1 on multiple benchmarks. However, the values of NMSE and SLR on all the benchmarks are significantly better (often the best) than S_1 and S_3.

RIS - S_5: We can see that S_5 entirely fails to reproduce most of the benchmarking patterns. The visual quality is the worst because the RIS lacks the beam steering capability under the planewave source assumption. The quantitative values of S_5 are also the worst. In B_7, the DE is close to 0, but NMSE and SLR are still the worst. The better value of DE for B_7, which has eight beams, is due to unintentional scattering in every direction by this surface, and the poor performance becomes evident when the error of unintended directions is considered through NMSE and SLR values. The same is true for B_8 where SLR is good, but the other two metrics are the worst.

2) PERFORMANCE WITH $G = 2$: WITH UNIT CELL GROUPING

When we group the unit cells in pairs ($G = 2$), the performance of all the RISs under planewave source assumptions further decreases. As shown in the bottom half of Table 3, the performance of RISs S_1 and S_2 gets more degraded than RISs S_3 and S_4, while the performance of S_5 is still the worst. The distinction between 1-bit and 2-bit unit cells and the effect of the unit cell radiation response are more prominent in dictating the RIS beam steering capability under planewave source assumptions. In case 2, optimizing a unit cell so that it produces maximally apart phase shifts in different control states also becomes crucial in obtaining good performance.

C. DISCUSSION AND COMPARISON

In Figure 8, we present the visual quality of the radiation pattern produced by S_1 (1-bit unit cell) while reproducing the benchmarking pattern B_4 under point/planewave source assumptions with $G = 1, 2$. We can see that we obtain the best result under the point source assumption with $G = 1$, which means that all the 1600 1-bit unit cells on the RIS have a separate control. On the other hand, when $G = 2$, under point source assumptions, the ability of the surface to reproduce the given pattern is severely degraded with a significant amount of power in several unwanted directions. Under planewave source assumptions and with $G = 1$, the quantization lobes are visible along with all the desired main

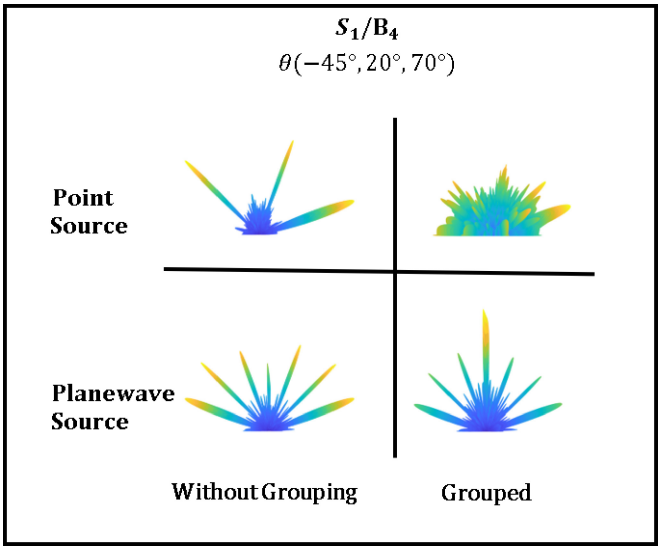

FIGURE 8. Radiation patterns generated by S_1 (1-bit unit cell) while reproducing the benchmarking pattern B_4 under point/planewave source assumptions with $G = 1, 2$.

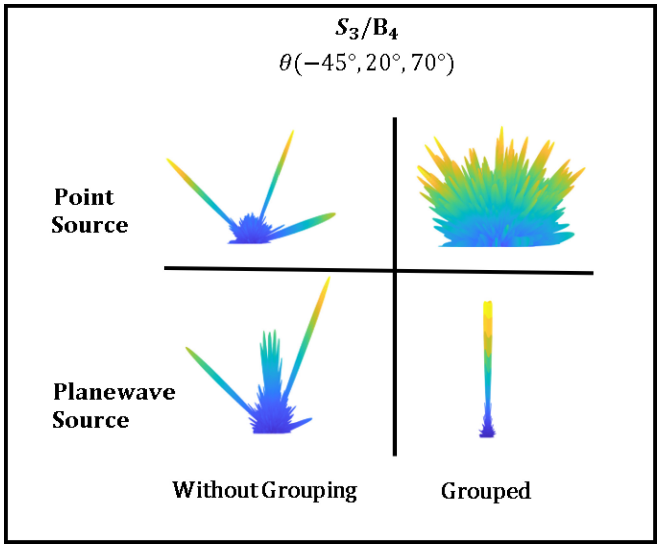

FIGURE 9. Radiation patterns generated by S_3 (2-bit unit cell) while reproducing the benchmarking pattern B_4 under point/planewave source assumptions with $G = 1, 2$.

lobes. With $G = 2$, the performance further degrades under the planewave source assumption.

In Figure 9, we present the visual quality of the radiation pattern produced by S_3 (2-bit unit cell) while reproducing the benchmarking pattern B_4 under point/planewave source assumptions with $G = 1, 2$. With $G = 1$ under the point source assumption, the three beams are visible. In this case, the power radiated in the unintended directions is relatively less than that radiated by S_1. With $G = 2$, the performance significantly degrades under the point source assumption, and it becomes equally bad, as we observe in the case for S_1. With $G = 1$ under planewave source assumptions, the performance of S_3 is comparable to the point source case because two out of three main lobes are visible and unlike S_1, there are no quantization lobes. Finally, with $G = 2$ under planewave source assumptions, S_3 loses its beam steering capability and cannot form any of the major lobes.

VI. CONCLUSION

We conducted a detailed analysis of the performance aspects of RISs composed of various unit cell designs. We developed a benchmarking framework that includes radiation patterns commonly required in a smart city environment. We presented performance metrics to quantify RIS radiation pattern generation capabilities relative to the benchmarking patterns, control circuit complexity, and power requirements for point/planewave source assumptions. Using this framework, we tested and compared five different RISs (S_1-S_5) made up of five different unit cell designs. The proposed framework can be handy for choosing unit cells from existing designs in various application settings and source type assumptions. We can also use the framework to determine the usefulness of future designs and their most viable applications. With the help of the proposed framework, we can also determine the optimal unit cell group size for the best tradeoff that favors ease of implementation and reduces the channel sensing overhead. A better understanding of the unit cell and surface-level RIS design interplay through the proposed framework will lead to better strategies for system-level performance enhancement in RIS-assisted communications.

ACKNOWLEDGMENT

Any opinions, findings and conclusions or recommendations expressed in this material are those of the author(s) and do not reflect the views of the Ministry of Education, Singapore. Any opinions, findings and conclusions or recommendations expressed in this material are those of the author(s) and do not reflect the views of A*STAR.

REFERENCES

[1] C. Huang, A. Zappone, G. C. Alexandropoulos, M. Debbah, and C. Yuen, "Reconfigurable intelligent surfaces for energy efficiency in wireless communication," *IEEE Trans. Wireless Commun.*, vol. 18, no. 8, pp. 4157–4170, Aug. 2019.

[2] J. Xu et al., "Reconfiguring wireless environments via intelligent surfaces for 6G: Reflection, modulation, and security," *Sci. China Inf. Sci.*, vol. 66, no. 3, 2023, Art. no. 130304.

[3] M. Jian et al., "Reconfigurable intelligent surfaces for wireless communications: Overview of hardware designs, channel models, and estimation techniques," *Intell. Converg. Netw.*, vol. 3, no. 1, pp. 1–32, Mar. 2022.

[4] J. An, C. Yuen, C. Huang, M. Debbah, H. V. Poor, and L. Hanzo, "A tutorial on holographic MIMO communications—Part I: Channel modeling and channel estimation," *IEEE Commun. Lett.*, vol. 27, no. 7, pp. 1664–1668, Jul. 2023.

[5] J. An, C. Yuen, C. Huang, M. Debbah, H. V. Poor, and L. Hanzo, "A tutorial on holographic MIMO communications—Part II: Performance analysis and holographic beamforming," *IEEE Commun. Lett.*, vol. 27, no. 7, pp. 1669–1673, Jul. 2023.

[6] J. An, C. Yuen, C. Huang, M. Debbah, H. V. Poor, and L. Hanzo, "A tutorial on holographic MIMO communications—Part III: Open opportunities and challenges," *IEEE Commun. Lett.*, vol. 27, no. 7, pp. 1674–1678, Jul. 2023.

[7] G. C. Alexandropoulos, K. Stylianopoulos, C. Huang, C. Yuen, M. Bennis, and M. Debbah, "Pervasive machine learning for smart radio environments enabled by reconfigurable intelligent surfaces," *Proc. IEEE*, vol. 110, no. 9, pp. 1494–1525, Sep. 2022.
[8] J. An et al., "Stacked intelligent metasurfaces for efficient holographic MIMO communications in 6G," *IEEE J. Sel. Areas Commun.*, early access, Jun. 21, 2023, doi: 10.1109/JSAC.2023.3288261.
[9] B. Yang et al., "Reconfigurable intelligent computational surfaces: When wave propagation control meets computing," *IEEE Wireless Commun.*, vol. 30, no. 3, pp. 120–128, Jun. 2023.
[10] M. Di Renzo et al., "Smart radio environments empowered by reconfigurable intelligent surfaces: How it works, state of research, and the road ahead," *IEEE J. Sel. Areas Commun.*, vol. 38, no. 11, pp. 2450–2525, Nov. 2020.
[11] Q. Wu, S. Zhang, B. Zheng, C. You, and R. Zhang, "Intelligent reflecting surface-aided wireless communications: A tutorial," *IEEE Trans. Commun.*, vol. 69, no. 5, pp. 3313–3351, May 2021.
[12] L. Wei, C. Huang, G. C. Alexandropoulos, C. Yuen, Z. Zhang, and M. Debbah, "Channel estimation for RIS-empowered multi-user MISO wireless communications," *IEEE Trans. Commun.*, vol. 69, no. 6, pp. 4144–4157, Jun. 2021.
[13] C. A. Balanis, *Antenna Theory Analysis and Design*, 4th ed. Hoboken, NJ, USA: Wiley, 2016.
[14] M. Di Renzo, F. H. Danufane, X. Xi, J. De Rosny, and S. Tretyakov, "Analytical modeling of the path-loss for reconfigurable intelligent surfaces–anomalous mirror or scatterer?" in *Proc. IEEE 21st Int. Workshop Signal Process. Adv. Wireless Commun. (SPAWC)*, 2020, pp. 1–5.
[15] F. H. Danufane, M. Di Renzo, J. De Rosny, and S. Tretyakov, "On the path-loss of reconfigurable intelligent surfaces: An approach based on Green's theorem applied to vector fields," *IEEE Trans. Commun.*, vol. 69, no. 8, pp. 5573–5592, Aug. 2021.
[16] X. Wei, L. Dai, Y. Zhao, G. Yu, and X. Duan, "Codebook design and beam training for extremely large-scale RIS: Far-field or near-field?" *China Commun.*, vol. 19, no. 6, pp. 193–204, 2022.
[17] M. Di Renzo et al., "Digital reconfigurable intelligent surfaces: On the impact of realistic reradiation models," 2022, *arXiv:2205.09799*.
[18] H. Yang et al., "A programmable metasurface with dynamic polarization, scattering and focusing control," *Sci. Rep.*, vol. 6, no. 1, pp. 1–11, 2016.
[19] X. Wan, M. Q. Qi, T. Y. Chen, and T. J. Cui, "Field-programmable beam reconfiguring based on digitally-controlled coding metasurface," *Sci. Rep.*, vol. 6, no. 1, pp. 1–8, 2016.
[20] L. Dai et al., "Reconfigurable intelligent surface-based wireless communications: Antenna design, prototyping, and experimental results," *IEEE Access*, vol. 8, pp. 45913–45923, 2020.
[21] Q. Ma, G. D. Bai, H. B. Jing, C. Yang, L. Li, and T. J. Cui, "Smart metasurface with self-adaptively reprogrammable functions," *Light Sci. Appl.*, vol. 8, no. 1, pp. 1–12, 2019.
[22] G. Bacci, L. Sanguinetti, and E. Björnson, "Spherical wavefronts improve MU-MIMO spectral efficiency when using electrically large arrays," *IEEE Wireless Commun. Lett.*, vol. 12, no. 7, pp. 1219–1223, Jul. 2023.
[23] C. Huang et al., "Holographic MIMO surfaces for 6G wireless networks: Opportunities, challenges, and trends," *IEEE Wireless Commun.*, vol. 27, no. 5, pp. 118–125, Oct. 2020.
[24] J. C. Liang et al., "An angle-insensitive 3-bit reconfigurable intelligent surface," *IEEE Trans. Antennas Propag.*, vol. 70, no. 10, pp. 8798–8808, Oct. 2022.
[25] Z. X. Wang, Q. Cheng, and T. J. Cui, "A reconfigurable 4-bit antenna element for beam-scanning application," in *Proc. IEEE 10th Asia–Pac. Conf. Antennas Propag. (APCAP)*, 2022, pp. 1–2.
[26] S. Zeng et al., "Intelligent omni-surfaces: Reflection-refraction circuit model, full-dimensional beamforming, and system implementation," *IEEE Trans. Commun.*, vol. 70, no. 11, pp. 7711–7727, Nov. 2022.
[27] H. Zhang and B. Di, "Intelligent omni-surfaces: Simultaneous refraction and reflection for full-dimensional wireless communications," *IEEE Commun. Surveys Tuts.*, vol. 24, no. 4, pp. 1997–2028, 4th Quart., 2022.
[28] M. Di Renzo, F. H. Danufane, and S. Tretyakov, "Communication models for reconfigurable intelligent surfaces: From surface electromagnetics to wireless networks optimization," *Proc. IEEE*, vol. 110, no. 9, pp. 1164–1209, Sep. 2022.
[29] H. Kamoda, T. Iwasaki, J. Tsumochi, T. Kuki, and O. Hashimoto, "60-GHz electronically reconfigurable large reflectarray using single-bit phase shifters," *IEEE Trans. Antennas Propag.*, vol. 59, no. 7, pp. 2524–2531, Jul. 2011.
[30] J.-H. Lim, G.-T. Back, Y.-I. Ko, C.-W. Song, and T.-Y. Yun, "A reconfigurable PIFA using a switchable PIN-diode and a fine-tuning varactor for USPCS/WCDMA/m-WiMAX/WLAN," *IEEE Trans. Antennas Propag.*, vol. 58, no. 7, pp. 2404–2411, Jul. 2010.
[31] R. Fara, P. Ratajczak, D.-T. Phan-Huy, A. Ourir, M. Di Renzo, and J. De Rosny, "A prototype of reconfigurable intelligent surface with continuous control of the reflection phase," *IEEE Wireless Commun.*, vol. 29, no. 1, pp. 70–77, Feb. 2022.
[32] H. Zhang, B. Di, L. Song, and Z. Han, "Reconfigurable intelligent surfaces assisted communications with limited phase shifts: How many phase shifts are enough?" *IEEE Trans. Veh. Technol.*, vol. 69, no. 4, pp. 4498–4502, Apr. 2020.
[33] W. Tang et al., "Path loss modeling and measurements for reconfigurable intelligent surfaces in the millimeter-wave frequency band," *IEEE Trans. Commun.*, vol. 70, no. 9, pp. 6259–6276, Sep. 2022.
[34] W. Tang et al., "Wireless communications with reconfigurable intelligent surface: Path loss modeling and experimental measurement," *IEEE Trans. Wireless Commun.*, vol. 20, no. 1, pp. 421–439, Jan. 2021.
[35] B. G. Kashyap, P. C. Theofanopoulos, Y. Cui, and G. C. Trichopoulos, "Mitigating quantization lobes in mmWave low-bit reconfigurable reflective surfaces," *IEEE Open J. Antennas Propag.*, vol. 1, pp. 604–614, 2020.
[36] M. Smith and Y. Guo, "A comparison of methods for randomizing phase quantization errors in phased arrays," *IEEE Trans. Antennas Propag.*, vol. AP-31, no. 6, pp. 821–828, Nov. 1983.

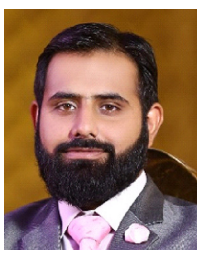

AMMAR RAFIQUE received the B.S. degree in electrical engineering from UET Lahore in 2015, and the M.S. degree in electrical engineering program from NUCES Lahore in 2018. His master's thesis was on machine learning-based automated fault diagnosis of synchronous machines, which heavily relied on EM simulation tools. In 2018, he joined as a Visiting Faculty Lab Instructor with NUCES Lahore, which he continued for a year. In 2019, he joined the Ph.D. program with ITU Lahore as a Full-Time Ph.D. Graduate Fellow. At MicroNano Lab, he has been working on reconfigurable intelligent surfaces with the help of various EM simulation tools. His research interests include communication systems, computer networks, and smart grids. He is a student member of the SPIE and OPTICA Societies and also a Young Professional Member of IEEE and manages social media pages of the IEEE APS/CAS/MTT/SSC Joint Chapter of the Lahore section (Region 10).

NAVEED UL HASSAN (Senior Member, IEEE) received the B.E. degree from the College of Aeronautical Engineering, Risalpur, Pakistan, in 2002, and the M.S. and Ph.D. degrees from the Ecole Superieure d'Electricite, Gif-sur-Yvette, France, in 2006 and 2010, respectively. He is an Associate Professor of Electrical Engineering with the Lahore University of Management Sciences, Pakistan. He has completed several impactful research projects and published over 100 research papers at international journals or conferences. His research interests include wireless communication, smart energy systems, blockchain technology, and indoor positioning systems. He serves as an Associate Editor for *Nature Computer Science* (Springer) and *IET Smart Grid*.

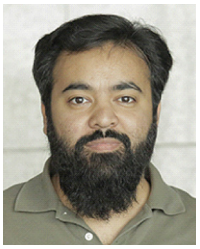

MUHAMMAD ZUBAIR (Senior Member, IEEE) received the Ph.D. degree in computational electromagnetics from the Polytechnic University of Turin, Italy. He is currently associated with the Innovative Technologies Laboratories, King Abdullah University of Science and Technology (KAUST) as a Research Scientist. Before joining KAUST, he was working as an Associate Professor and the Chair with the Department of Electrical Engineering, Information Technology University, Lahore. Before joining ITU, he was a Postdoctoral Research Fellow with SUTD-MIT International Design Centre, Singapore. His Ph.D. research was carried out at Antenna and EMC Lab, Istituto Superiore Mario Boella, in Turin, Italy, where he worked on computational EM projects funded by Army Research Lab in collaboration with Boston University, USA. During his postdoctoral, he has been working on various research projects related to fractional methods in electromagnetics funded by the Air Force Office of Scientific Research/Asian Office of Aerospace Research and Development and Singapore Temasek Laboratories. He is a Principal author of his book on *Electromagnetic Fields and Waves in Fractional Dimensional Space*, published by (Springer, NY, USA). He has contributed over 50 scientific works in journals and conferences of international repute. He has been selected for the 'URSI Young Scientist Award' in the URSI General Assembly (GASS) in 2021 and has been awarded Punjab Innovation Research Challenge Award in 2021. He has been an Associate Editor of the IEEE ACCESS and an Editorial Board Member for the *IET Microwaves, Antennas & Propagation*, *PLOS One*, and *International Journal of Antennas and Propagation*. He continues to serve the scientific community as an Invited Book Reviewer for *Contemporary Physics* (Taylor & Francis).

IJAZ HAIDER NAQVI (Senior Member, IEEE) received the B.Sc. degree in electrical engineering from the University of Engineering and Technology Lahore, Pakistan, in 2003, the master's degree in radio communications from the Ecole Superieure d'Electricite (SUPELEC), Gif-sur-Yvette, France, in 2006, and the Ph.D. degree in electronics and telecommunication engineering from Institut National des Sciences Appliquées, Rennes, France, in 2009. He is an Associate Professor of Electrical Engineering with the Lahore University of Management Sciences, Lahore, Pakistan. He was a Visiting Associate Professor with the University of Maryland College Park in 2019. He has published over 70 papers in top-ranked international journals and conferences. His research interests include next-generation wireless, multi-antenna, battery energy storage systems, and prognostics and health management of lithium-ion batteries.

MUHAMMAD QASIM MEHMOOD (Senior Member, IEEE) received the Ph.D. degree from the National University of Singapore in 2016. He is currently working as an Associate Professor with the Department of Electrical Engineering, Information Technology University, Lahore, Pakistan. His research interests include metaoptics and metaphotonics, optical and photonics engineering, antenna and microwave engineering, and printed electronics. He is the Director of MicroNano Lab with ITU and supervised/co-supervised several undergraduate and graduate Thesis. He has been listed among the top 2% of scientists in a global list (of 2021 and 2022) released by Stanford University. He is the recipient of the 2023 ICO/ICTP Gallieno Denardo Award for his remarkable contributions to the field of Nano-optics and Meta-Photonics; and for inspiring many young researchers in Pakistan through quality research, mentorship, community services, and outreach activities. He secured several grants from various national and international funding agencies. He is the Chair of the IEEE APS/CAS/MTT/SSC Joint Chapter of the Lahore section (Region 10) and an Advisor of ITU's SPIE and OPTICA Chapters. He works closely with other national and international societies to promote science by organizing various student development and outreach programs like symposiums, seminars, internships, project competitions, and awareness sessions. The prime focus is to target the unprivileged sections of society in Pakistan's far-reach low resources to promote science and encourage/expose students of all genders to science education. His efforts are helping immensely in advancing science and producing internationally competitive researchers from Pakistan. He is a member of the Pak-ICTP Alumni Society.

MARCO DI RENZO (Fellow, IEEE) received the Laurea (cum laude) and Ph.D. degrees in electrical engineering from the University of L'Aquila, Italy, in 2003 and 2007, respectively, and the Habilitation à Diriger des Recherches (Doctor of Science) degree from University Paris-Sud (currently Paris-Saclay University), France, in 2013. He is currently a CNRS Research Director (Professor) and the Head of the Intelligent Physical Communications Group, Laboratory of Signals and Systems, Paris-Saclay University–CNRS and CentraleSupelec, Paris, France. At Paris-Saclay University, he serves as the Coordinator of the Communications and Networks Research Area of the Laboratory of Excellence DigiCosme, as a Member of the Admission and Evaluation Committee of the Ph.D. School on Information and Communication Technologies, and as a Member of the Evaluation Committee of the Graduate School in Computer Science. He is a Founding Member and the Academic Vice Chair of the Industry Specification Group on Reconfigurable Intelligent Surfaces within the European Telecommunications Standards Institute, where he serves as the Rapporteur for the work item on communication models, channel models, and evaluation methodologies. Also, he holds the 2023 France-Nokia Chair of Excellence in ICT, and was a Fulbright Fellow at City University of New York, USA, a Nokia Foundation Visiting Professor, and a Royal Academy of Engineering Distinguished Visiting Fellow. His recent research awards include the 2021 EURASIP Best Paper Award, the 2022 IEEE COMSOC Outstanding Paper Award, the 2022 Michel Monpetit Prize conferred by the French Academy of Sciences, the 2023 EURASIP Best Paper Award, the 2023 IEEE ICC Best Paper Award (wireless), the 2023 IEEE COMSOC Fred W. Ellersick Prize, the 2023 IEEE COMSOC Heinrich Hertz Award, and the 2023 IEEE VTS James Evans Avant Garde Award. He served as the Editor-in-Chief for IEEE COMMUNICATIONS LETTERS from 2019 to 2023 and is currently serving in the Advisory Board. He is a Fellow of IET and AAIA; an Ordinary Member of the European Academy of Sciences and Arts, an Ordinary Member of the Academia Europaea; and a Highly Cited Researcher.

MÉROUANE DEBBAH (Fellow, IEEE) is a Researcher, an Educator and a Technology Entrepreneur. Over his career, he has founded several public and industrial research centers, start-ups and is currently a Professor with the Khalifa University of Science and Technology, Abu Dhabi, and the Founding Director of the 6G Center. His research has been lying at the interface of fundamental mathematics, algorithms, statistics, information and communication sciences with a special focus on random matrix theory and learning algorithms. In the Communication field, he has been at the heart of the development of small cells (4G), Massive MIMO (5G), and Large Intelligent Surfaces (6G) technologies. In the AI field, he is known for his work on large language models, distributed AI systems for networks and semantic communications. He received multiple prestigious distinctions, prizes, and best paper awards (more than 35 best paper awards) for his contributions to both fields and according to research.com is ranked as the Best Scientist in France in the field of Electronics and Electrical Engineering. He is a Frequent Keynote Speaker at international events in the field of telecommunication and AI. He is a WWRF Fellow, a Eurasip Fellow, an AAIA Fellow, an Institut Louis Bachelier Fellow, and a Membre émérite SEE.

CHAU YUEN (Fellow, IEEE) received the B.Eng. and Ph.D. degrees from Nanyang Technological University, Singapore, in 2000 and 2004, respectively.

He was a Postdoctoral Fellow with Lucent Technologies Bell Labs, Murray Hill, in 2005, and a Visiting Assistant Professor with The Hong Kong Polytechnic University in 2008. From 2006 to 2010, he was with the Institute for Infocomm Research, Singapore. From 2010 to 2023, he was with the Engineering Product Development Pillar, Singapore University of Technology and Design. Since 2023, he has been with the School of Electrical and Electronic Engineering, Nanyang Technological University. He has 3 U.S. patents and published over 500 research papers at international journals or conferences.

Dr. Yuen received IEEE ICC Best Paper Award in 2023, the IEEE Communications Society Fred W. Ellersick Prize in 2023, the IEEE Marconi Prize Paper Award in Wireless Communications in 2021, and the EURASIP Best Paper Award for Journal on Wireless Communications and Networking in 2021. He was a recipient of the Lee Kuan Yew Gold Medal, the Institution of Electrical Engineers Book Prize, the Institute of Engineering of Singapore Gold Medal, the Merck Sharp and Dohme Gold Medal, and twice a recipient of the Hewlett Packard Prize. He received the IEEE Asia–Pacific Outstanding Young Researcher Award in 2012 and IEEE VTS Singapore Chapter Outstanding Service Award in 2019. He currently serves as an Editor-in-Chief for *Nature Computer Science* (Springer), an Editor for IEEE TRANSACTIONS ON VEHICULAR TECHNOLOGY, IEEE SYSTEM JOURNAL, and IEEE TRANSACTIONS ON NETWORK SCIENCE AND ENGINEERING, where he was awarded as the IEEE TNSE Excellent Editor Award and a Top Associate Editor for TVT from 2009 to 2015. He also served as a Guest Editor for several special issues, including IEEE JOURNAL ON SELECTED AREAS IN COMMUNICATIONS, *IEEE Wireless Communications Magazine*, *IEEE Communications Magazine*, *IEEE Vehicular Technology Magazine*, IEEE TRANSACTIONS ON COGNITIVE COMMUNICATIONS AND NETWORKING, and *Applied Energy* (Elsevier). He is a Distinguished Lecturer of the IEEE Vehicular Technology Society, Top 2% Scientists by Stanford University, and also a Highly Cited Researcher by Clarivate Web of Science.